Implementation of vibration correction schemes to the evaluation of a turbulent flow in an open channel by tomographic particle image velocimetry

Thomas Earl, Steve Cochard, Lionel Thomas, Benoit Tremblais, Laurent David

Implementation of vibration correction schemes to the evaluation of a turbulent flow in an open channel by tomographic particle image velocimetry

T A Earl[1,2], S Cochard[2], L Thomas[1], B Tremblais[3] and L David[1]

[1] Pprime, CNRS, ENSMA, University of Poitiers, 86962 Futuroscope Cédex, France
[2] School of Civil Engineering, The University of Sydney, NSW 2006, Australia
[3] Xlim Laboratory, SIC Department, University of Poitiers, CNRS 7252, 86962 Futuroscope Cédex, France

E-mail: thomas.earl@univ-poitiers.fr

Abstract

The aim of this paper is to investigate and quantify the effect of vibration on exp tomographic particle image velocimetry (TPIV) measurements. The experiment consisted of turbulence measurements in an open channel flow. Specifically, five trash rack assemblies, composed of regular grids, divided a 5 m long flume into four sequential, identical pools. This set-up established a globally stationary flow, with each pool generating a controlled amount of turbulence that is reset at every trash rack. TPIV measurements were taken in the central pool. To eliminate the vibration from the measurements, three vibration correction regimes are proposed and compared to a global volume self-calibration (Wieneke 2008 *Exp. Fluids* **45** 549–56), a now standard calibration procedure in TPIV. As the amplitude of the vibrations was small, it was possible to extract acceptable reconstruction re-projection qualities ($Q_I > 75\%$) and velocity fields from the standard treatment. This paper investigates the effect of vibration on the cross-correlation signal and turbulence statistics, and shows the improvement to velocity field data by several correction schemes. A synthetic model was tested that simulated camera vibration to demonstrate its effects on key velocity parameters and to observe the effects on reconstruction and cross-correlation metrics. This work has implications for experimental measurements where vibrations are unavoidable and seemingly undetectable such as those in large open channel flows.

Keywords: vibration correction, volume self-calibration, open channel flow, tomographic PIV

1. Introduction

The aim of this work is to characterise and correct the effect of camera vibration on tomographic particle image velocimetry (TPIV) measurements made in a turbulent, open channel flow. The flume used in this investigation was specifically designed to control the mean flow properties, such as bulk velocity, vortex production and energy dissipation. To this end, the inclined open channel flow was divided into sequential pools by a series of trash racks, or regular grids, to simulate the turbulent flow that can be found in rivers (figure 1). The intended application of this flow type is to mimic the turbulence and flow conditions that fish may encounter in rivers or vertical slot fishways. Future investigations will evaluate the swimming capability of various species of fish after the full flow characterisation of the channel.

There are two primary challenges involved with measuring turbulence in the flows found in open channel flows. Firstly, to

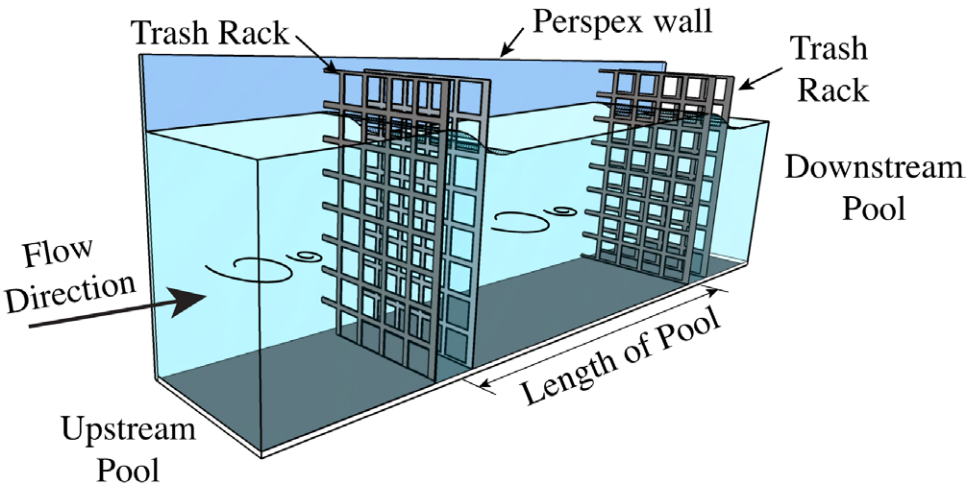

Figure 1. Cut-away schematic of one of a series of pools in the flume used in the experiments. The flow conditions are periodic across the pools: the flow is reset at each trash rack, highlighted by the idealised evolution of the vortices. Note that the fine wire meshes upstream of the trash racks are not shown here for greater clarity.

ensure that the flow conditions in the apparatus are equivalent to those typically found in the field, a large experimental rig is required to achieve a high Reynolds number. In addition, to maintain Froude similitude, any scaled model requires proportionally higher flow rates. Thus, the combination of relatively large geometry with high flow rates can cause vibration of the rig and/or measurement equipment. Secondly, the flow is characterised by a highly unsteady free surface that entrains air. This entrainment generates bubbles that can hinder the use of optical techniques.

The flow characteristics that are most significant to the migration of fishes inside open channel flows are large, persistent vortices that occur at the length scale in the order of the species sizes and the turbulent kinetic energy of the flow. Large scale vortices can destabilise fish and excessive turbulent kinetic energy in the flow can induce fatigue in the fish, making upstream progress more difficult (Lacey *et al* 2012, Calluaud *et al* 2014). It was therefore not a primary objective of these turbulence measurements to resolve the Kolmogorov length scales to fully resolve the flow. In this study, it was of greater importance to measure the larger scale vortices and flow field. Therefore, to completely characterise the vortices and structure of turbulent flow, a three component (3C), three-dimensional (3D) technique where the full velocity gradient tensor was required.

TPIV (Elsinga *et al* 2006) is a 3D implementation of PIV that was employed to measure the flow in this investigation. TPIV utilises a number of simultaneously acquired particle images (typically four) to recover the 3D positions of the illuminated particles by projecting their images into the measurement volume. A comprehensive review of TPIV studies is given by Scarano (2013), showing the rapid growth in the technique's use over the last several years. For a greater technical insight, Thomas *et al* (2014) recently optimised a selection of parameters for TPIV algorithms. In this paper, the quantitative influence of correcting experimental measurements with a volume self-calibration (Wieneke 2008) and single-image vibration correction (Michaelis and Wolf 2011) is investigated. Apart from an investigation on volume self-calibration stability as a function of the number of cameras (Discetti *et al* 2013), there appears to be a scarcity of studies since then that have utilised a single-image vibration correction technique. Thus, several correction methods are applied and compared to understand the effect on the tomographic reconstructions of the particles, the signal to noise ratio of the correlations along with quantitative differences between the flow field divergence and turbulence statistics.

The paper is arranged as follows: the experimental apparatus is described along with the global analysis of the open channel flow in section 2, the TPIV set-up is described in section 3, the vibration correction procedures are addressed in section 4, the quantification of the corrected results and discussion are presented section 5 and include turbulence statistics such as vorticity levels and turbulent kinetic energy. To further investigate the effect of camera vibration, a synthetic model was tested that simulated camera vibration, which is presented in section 6. Finally, conclusions are drawn in section 7.

2. Experimental set-up and global flow properties

Experiments were conducted in an open channel (figure 2) at the Institut Pprime at the University of Poitiers, France. The inclined channel was rectangular in cross section with dimensions 500 × 304 mm (height, H × width, W) and had 30 mm thick perspex walls and base to allow full optical access. The channel was divided into four identical pools along its length that were separated by trash rack assemblies (section 2.1) to control the flow. This setup achieves a steady and periodic flow regime: that is, where the global properties of the flow in each pool are the same and constant over time. The water was pumped with a constant flow rate of $Q = 34$ L s^{-1} from the lower reservoir into the upper reservoir, which in turn propagated down the channel by gravity. The inclination of the channel was fixed at a slope of 5% . The height of the weir gate at the end of the flume was adjusted so that there was a constant head loss, ΔH across each trash rack (see figure 2).

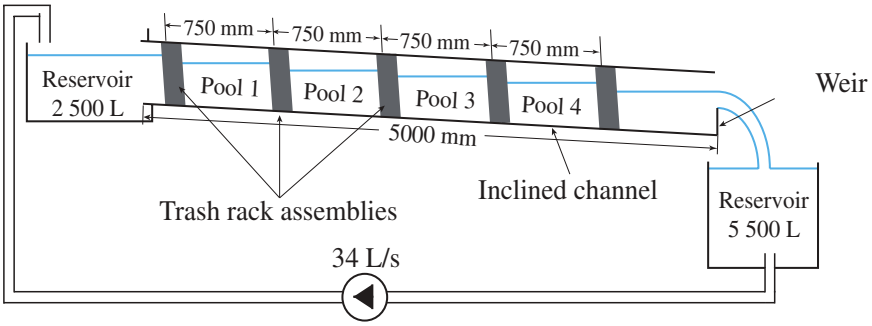

Figure 2. Schematic of inclined open channel, divided into four identical pools by five trash rack assemblies.

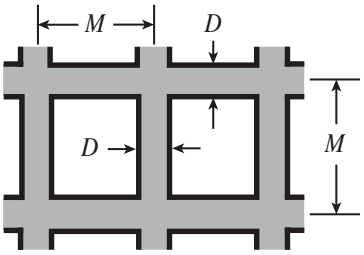

GRADES

Grid	M [mm]	D [mm]	σ
G1	12	2	0.31
G2	14	4	0.49

Figure 3. Grid geometries used in pairs to form the trash racks that divided the channel into pools.

2.1. Trash rack and grid details

Each pool was separated by a trash rack assembly that was angled toward the flow at 10%, relative to the normal of the channel bottom. The trash racks comprised, from upstream to downstream, a fine wire mesh and a pair of regular grids that were fabricated from 2 mm thick stainless steel plates. The function of the fine wire meshes was to ensure that any persisting large scale eddies from the upstream pool were broken up before entering the next pool, resetting the flow. This ensured that the influence of the turbulence in the pool generated further upstream was minimised. The fine wire mesh was composed of 0.4 mm diameter wire with approximately 2 mm spacing. The grid pairs used were G1 with G2 (G1G2) with open square geometries as shown in figure 3. The solidity ratios, defined by $\sigma = (D/M)(2 - D/M)$, are given in figure 3, where D is the width of each bar and M is the centre-to-centre bar spacing of the grid. The stream-wise spacing between the grids in the trash rack was 90 mm.

2.2. Bulk flow properties

The water temperature was 15.4 ± 0.5 °C, which was closely monitored. The hydraulic diameter, $D_H = h_c W/(2h_c + W)$, for this channel was in the order of 0.1 m, where h_c is the vertical flow depth at the centre of the pool. The bulk mean velocity of the flow through each pool, $U_0 = Q/(h_c W)$, was 0.35 m s^{-1}, corresponding to a Reynolds numbers, Re_{D_H} of 30 400. The flow was subcritical, with a Froude number $\mathrm{Fr} = U_0/\sqrt{gh_c} \approx 0.2$. The Reynolds number with respect to grid geometry, Re_M, was 4300.

2.3. Volumetric dissipated power and energy

The volumetric dissipated power P_V can be used to approximate the global flow features in flume. From this metric, the dissipative (Kolmogorov) microscales of the flow can also be approximated. The microscales define the smallest scales in a turbulent flow where viscous effects dominate and convert turbulence kinetic energy into heat through dissipation. To achieve a fully resolved flow, the resolution of the measurement system must be fine enough to capture them (Tanaka and Eaton 2007). The P_V in a pool, per unit volume, can be estimated by computing the ratio of the work done to the volume of water in the pool:

$$P_V = \frac{\rho g Q \Delta H_B}{LWh_c} = \epsilon_0 \rho \tag{1}$$

where ρ is the density of water, g is gravity and L is the length of the pool, taken to be the centre-to-centre distance between sequential trash racks. By applying Bernoulli's equation (equation (2)) between the centre points of two successive pools, it is possible to approximate the bulk head loss ΔH_B:

$$\frac{p_1}{\rho g} + \frac{U_1^2}{2g} + z_1 = \frac{p_2}{\rho g} + \frac{U_2^2}{2g} + z_2 + \Delta H_B \tag{2}$$

where the pressure p is the same in successive pools and identically the velocity $U_1 = U_2 = U_0$. Therefore, ΔH_B is directly proportional to the change in elevation $z_1 - z_2$. The bulk dissipated energy ϵ_0 can then be computed from equation (1), which is used to approximate the Kolmogorov length scale: $\eta = (\nu^3/\epsilon_0)^{1/4}$, where ν is the kinematic viscosity of water. Table 1 summarises the results of this analysis.

Table 1. Properties of the flow estimated from the bulk analysis for each grid combination.

Case	G1G2
h_c	320 mm
ΔH	60 mm
P_V	171 Wm^{-3}
η	0.067 mm

2.4. 2D PIV

To gain a greater insight into the global flow, a two component, two-dimensional (2C–2D) PIV study of the flow in pool 3 (the same pool that the TPIV measurements were taken, section 3.1) was conducted. For the purposes of this article, this 2D PIV analysis serves to show the mean flow field which in the central, lengthwise plane of the pool.

Figure 4 shows the contour map of mean streamwise component of velocity U normalised by U_0, realised from an average of 500 fields, with bulk flow direction from left to right. One out of every 100 velocity vectors is displayed to aid visualisation of the flow field. The blue box in the figure indicates the location of the TPIV measurements. Contour lines of $U - U_0$ between −0.010 and 0.025 m s^{-1} were added for $x > 100$ mm to highlight the flow pattern in the centre of the pool. In particular, a stronger undercurrent at $y = 50$ mm for $x < 400$ mm persists into the TPIV measurement region. This field also shows a high velocity region near the free surface caused by its plunging action after passing through the trash rack assembly. The flow can be seen to accelerate towards the end of the pool owing the contraction in the channel cross-section by the trash rack housing. The dark blue region propagating from the origin is a recirculation zone, resulting from the bottom of the trash rack housing ending (akin to a flow over a backward facing step). Finally, the jetting of the flow through the grids can also be observed at the entrance to the pool.

3. TPIV set-up

TPIV follows a procedure that involves camera calibration, image acquisition, image processing, reconstruction of particle intensities in a computational volume and calculation of volumetric velocity fields (Elsinga *et al* 2006). This section describes the optimisation of the TPIV parameters used in this study. The tomographic reconstructions and correlations were made using the SLIP library developed at the University of Poitiers (Tremblais *et al* 2010).

3.1. TPIV system

TPIV measurements were taken in pool 3 to ensure that the flow was fully developed (figure 5). Four 1600 × 1200 px 8 bit CV-M2 JAI cameras were used to acquire the images. The cameras were positioned symmetrically in an inverted pyramid configuration, with declination and inward angles of approximately 20°. This positioning resulted in a camera angle subtended from the normal of the side walls of ∼30°. The camera orientation was a balance between approaching the optimum camera subtended angles for TPIV (shown to be between 30–45° for synthetic images, Thomas *et al* 2010, DeSilva *et al* 2011) and reducing the aberrations of the particle images due to the high refractive index change at the interface of the air and the channel. Water prisms can be used to negate the optical aberrations by ensuring the air-perspex interface is perpendicular to the camera lens axes, however they were not used in this study. This was due to the need to have unobstructed optical access in the whole pool, and the high complexity of the design and placement of the prisms, owing to the two 20° rotations in each plane.

All cameras were fitted with 50 mm lenses, 532 nm pass optical filters (corresponding to the laser frequency) and 2-axis lens mounted adapters, adjusted to achieve the Scheimpflug condition. Additionally, the apertures were set at $f\# = 22$ during acquisition for superior depth of field. Neutrally buoyant, spherical, polyamide particles[4] of mean diameter $d_{50} \approx 56\,\mu$m and density $\rho_p = 1.02$ g cm^{-3} were used to seed the flow. The average imaged particle diameter was $d_\tau \approx 5.5$ px, computed from an autocorrelation analysis of the image.

A double head Nd:YAG laser with 120 mJ per pulse was used to produce a 15 mm thick laser sheet (regulated with parallel plates) to illuminate the measurement volume. The laser and its optics were positioned under the channel, independent from the channel structure. This permitted the identical configuration of the four cameras to view the forward scattering of the seeding particles. The measurement volume in the centre of the pool was $100 \times 70 \times 12$ mm^3 ($x \times y \times z$) and aligned with the flow direction. The reduction of the reconstructed volume's domain was made to remove the effect of an impurity on the laser optics that had been found to reduce the laser intensity in a narrow band. The time step Δt between corresponding images was 2 ms, chosen to achieve mean particle displacements of ∼8 px on each camera. The resulting velocity fields were extracted at a frequency of 5 Hz.

3.2. Image processing

For each camera and for corresponding laser pulses, the median image from 50 sequential images was subtracted to remove the background noise. This method was shown to be more effective than local window filters, due to the nature of the background noise. The effect of image filtering is shown in figure 6. The processed images to be reconstructed had a homogeneous particle per pixel, ppp ≈ 0.03, or an image source density $N_s \approx 0.6$ (Scarano 2013), for all cameras at both time-steps. A gaussian filtering kernel was then applied to smooth particle images.

Small bubble entrainment in the water due to the free surface and subsequent turbulent mixing through the trash rack assembly was evident and detracted from the quality of the reconstruction (figure 6). The bubbles had two main effects: primarily, when illuminated, they created image 'particles' of diameter larger than the mean ($d_\tau \approx 10$ px) that were at times large enough to cause over exposure and an Airy disk effect on the images. The second problem was that the bubbles in the foreground, that is, between the illuminated volume and the camera (i.e. not illuminated directly by the laser volume)

[4] VESTOSINT 2157.

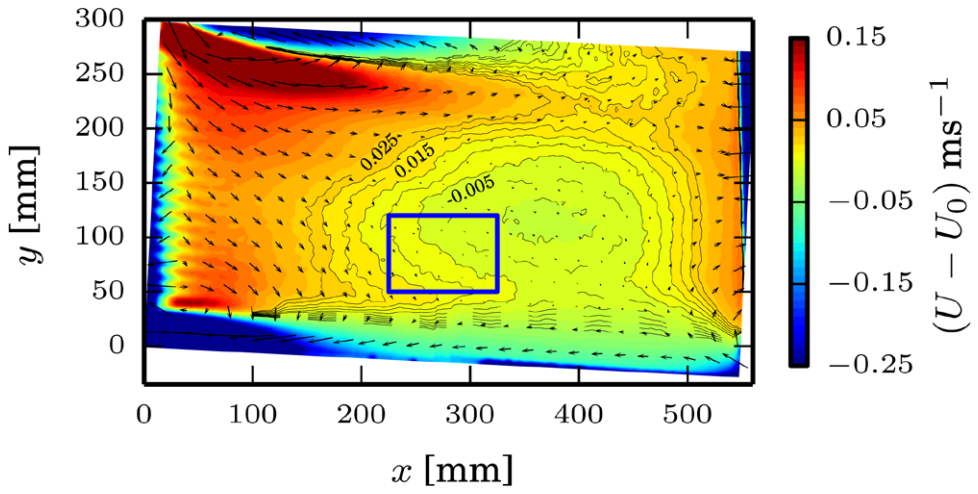

Figure 4. Mean 2D PIV flow field, averaged over 500 velocity fields. U is the mean component of velocity in the stream wise direction. Only every 100th vector is plotted. Contour lines ranging from $U - U_0$ between –0.010 and 0.025 m s^{-1} to highlight the flow in the centre of the pool.

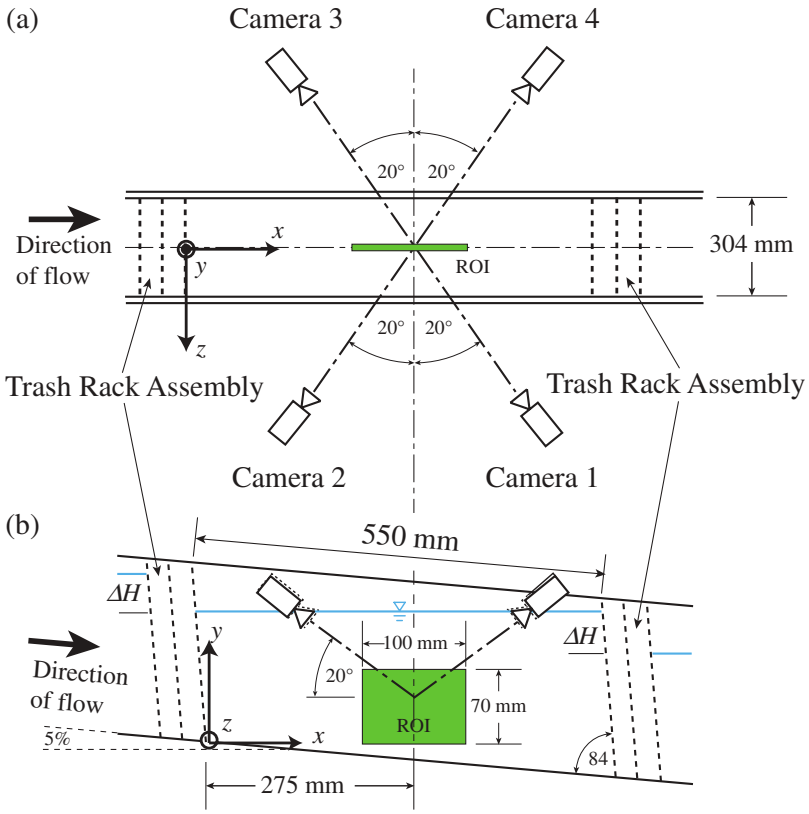

Figure 5. Schematic of Pool 3 showing measurement volume or region of interest (ROI) in (*a*) plan and (*b*) elevation. The origin and axis orientation along with inverted pyramid configuration of the cameras are shown.

perturbed the line-of-sight (LoS) of the particles and left regions in the images where there appeared to be no particles. No standard image treatment was able to rectify these effects, therefore if the reconstruction quality deteriorated below a threshold of 75%, the image sets were disregarded.

3.3. Volume reconstruction

The volume reconstruction parameters and methods for all of the vibration correction (section 4) schemes were kept identical. The reconstruction was split into a volume initialisation and volume reconstruction phase, with the aim of optimising the available reconstruction algorithms. The volume initialisation step was performed by a MinLOS (Putze and Maas 2008, Worth and Nickels 2008) that was proceeded by two iterations of SMART (Atkinson and Soria 2009). The SMART algorithm has been shown to perform faster than MART for reconstruction, however it also requires more iterations to obtain similar reconstructed volumes. SMART is therefore used to improve the quality of volume initialisation at minimum computational

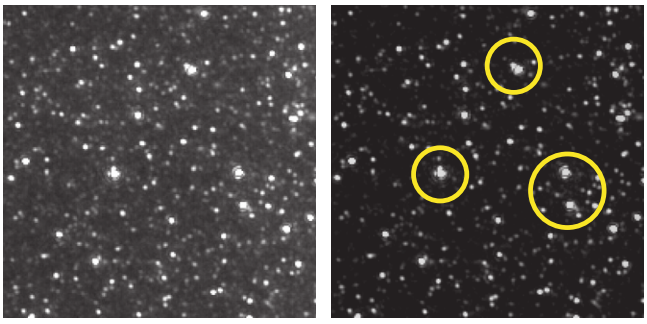

Figure 6. 200 × 200 px sample of (*a*) raw image and (*b*) after the median image subtraction. The yellow circles highlight large overexposed 'particle' images caused by small bubble entrainment.

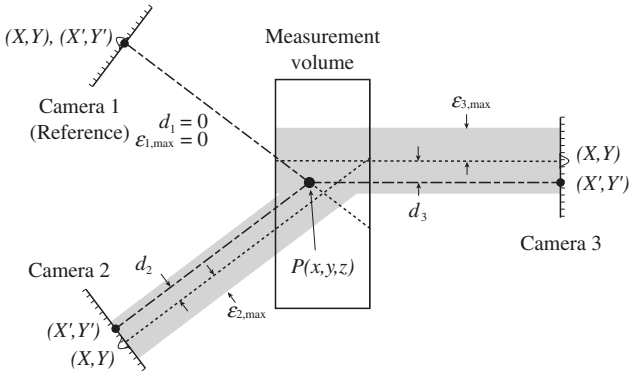

Figure 7. Volume-self calibration definitions. Without losing generality, three cameras are shown instead of the four used in this investigation. Additionally, the definitions are shown in an idealised 2D plane. The shaded grey regions denote the projection of the search area of radius $\varepsilon_{i,\max}$. Camera 1 is used as a reference camera.

cost, and to speed up convergence of the subsequent reconstruction algorithm. The volume reconstruction was computed with four iterations of the BiMART algorithm (Byrne 2009, Thomas *et al* 2014). The BiMART algorithm (equation (3)) can obtain reconstruction qualities similar to the MART algorithm but the division of the images $I(X_i)$ into *blocks* $\mathscr{B}$ permits greater computational efficiency. This is because rather than LoS calculations (particularly the calculation of non-zero voxels in a LoS, the $\sum_{j\in N_i} w_{i,j}E(x_j)$ term in equation (3)) being computed over each pixel, they are computed for each $\mathscr{B}$. Too large a $\mathscr{B}$ reduces the reconstructed volume quality; however, with $\mathscr{B} = 4 \times 4$ px, an equivalent volume can be obtained with few LoS calculations.

$$E(x_j)^{k+1} = E(x_j)^k \prod_{i\in\mathscr{B}}^{N_i} \left(\frac{I(X_i)}{\sum_{j\in N_i} w_{i,j} E(x_j)^k} \right)^{\mu w_{i,j}} \qquad (3)$$

where μ is a relaxation parameter which was set as a function of the number of iterations to maximise the reconstruction quality (Thomas *et al* 2014), $E(x_j)$ is the energy of the voxels, and $w_{i,j}$ is the weighting coefficient. A 2D gaussian filter was passed through each x–y voxel plane in the first two iterations and a volume thresholding was applied (Discetti and Astarita 2011). This increases the correlation quality with the effect of reducing ghost particles.

The volumes were reconstructed with a 15% enlargement in the z direction. This was to ensure that the ghost particles are distributed over a larger volume and to increase the signal to noise ratio. The enlarged portion of the reconstructed volume was then discarded so that only the particles reconstructed within the physical boundaries of the laser sheet were cross-correlated.

3.4. Velocity field calculation

A two-pass 64 × 64 × 64 voxel correlation volume with 75% overlap was used to find the most probable displacement of particles across the two reconstructed volumes. This resulted in 13 120 vectors per acquisition at a vector spacing of δx = 1.5 mm. A median vector replacement regime was implemented as per Westerweel and Scarano (2005). As tomographic reconstruction had been shown to be particularly susceptible to noise (Worth *et al* 2010), a bilateral filter was used to filter the velocity fields, which was preferred over a gaussian filter as it preserves edges. The vector spacing of the TPIV fields was in the order of 22η. To capture the Kolmogorov scale, the optimum vector spacing must have been $\eta/10 < \delta x < \eta/2$ (Tanaka and Eaton 2007). As mentioned in the introduction to this article, it is the larger scale structures in the flow that are of interest.

4. Volume self-calibration and vibration correction

The camera calibration mapping function M, which maps real-world coordinates to the camera image, is required to be accurate to within a fraction of a pixel (ideally 0.1 px or less) for a successful tomographic particle reconstructions (Wieneke 2008). During the experiments, the flume and camera rig vibrated unavoidably due to the energy of the flow which invalidated the camera mapping obtained from the camera calibration. This was despite the experimental rig being a solid construction of 80 × 80 mm^2 cross section extruded aluminium framing. All of the cameras were on a common rack that was securely fastened to the main frame of the flume. The two camera pairs were each on a section that cantilevered out from either side of the rig to allow optical access through the side walls of the flume. The laser and laser sheet optics were independent of these, positioned on the solid concrete floor beneath the flume. Single-image vibration correction was first proposed by Michaelis and Wolf (2011), utilising the volume self-calibration technique introduced by Wieneke (2008). The volume self-calibration technique performs a calibration on the particles themselves, in order to update M until the required mapping accuracy for TPIV is achieved.

To aid this discussion, figure 7 shows a 2D schematic of the definitions used in the volume self-calibration technique, shown with three rather than the four cameras used in this study for clarity. This camera system (X, Y) represents the location of a single particle identified on a camera image. $P(x, y, z)$ is the

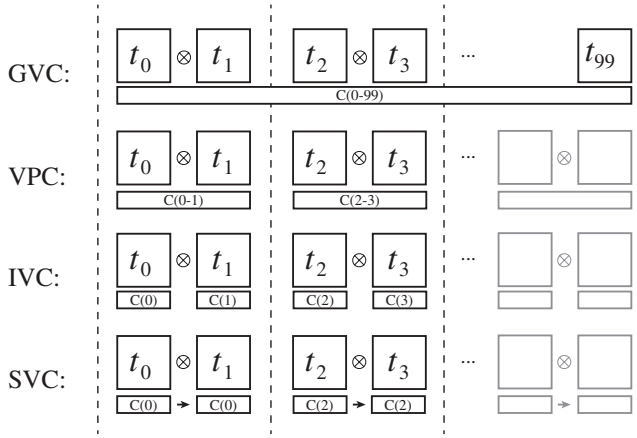

Figure 8. Volume self-calibration methods. C(i) indicates the time-step t_i on which the volume self-calibration is performed and likewise, C($i_1 - i_2$) indicates the range of time-steps.

point in the measurement volume, corresponding to the location of physical particle, whose location is determined by a 3D best-fit of the projections of (X, Y) from each camera. The particle candidates (X, Y) on the non-reference cameras are selected based on a triangulation regime (Maas *et al* 1993). For a given camera i, a disparity is defined as $d_i = (X, Y) - (X', Y')$, where (X', Y') is the projection of P onto the camera image from the mapping function, $(X', Y') = M_i \times P$. The corrected mapping function M'_i is computed by collecting all of the measured disparities d_i. In this analysis, the disparities were computed over a coarse grid of $n_x \times n_y \times n_z = 8 \times 8 \times 4$ sub-volumes. Each camera's mapping function is then updated by $M'_i(x, y, z) = M_i(x, y, z) - d_i(x, y, z)$.

To find a valid location for P, a search radius centred around (X, Y), otherwise known as the maximum allowed uncertainty $\varepsilon_{\max}$, is set to exceed the maximum expected disparities. The expected number of false matches (or ghost particles) is proportional to the particles per pixel and to $\varepsilon^5_{\max}$ (Wieneke 2008). The implementation of volume self-calibration used in this work utilises several techniques to obtain a maximum number of real particles. To remove noise and to avoid local bright or dark regions on the particle images, a local sliding mean filter followed by image thresholding was applied. 2D particles were then located on all images with a local peak detection—that is, a 2D particle is found when the centre pixel is the maximum of a 3 × 3 px sliding window. The 2D particles are sorted from brightest to dimmest, and triangulation to obtain 3D particle candidates is then performed, starting with the brightest particles. As an additional measure, a 3D particle candidate is only considered valid if it is unique on at least one 2D particle's line-of-sight. This step is to reduce the likelihood that it is a ghost particle. In this way, the volume is populated until the maximum number of 3D particles can be obtained without increasing the number of false matches.

4.1. Vibration-correction implementations

To quantify the effect of vibration correction techniques, four variations of the volume self-calibration were applied. These definitions are shown schematically in figure 8.

GVC Global Volume Correction: This is the standard implementation of the volume self calibration. The calibration model is generated by considering a large batch of images, in this case 100. The same calibration model is used for the reconstruction of all volumes as per the implementation of Wieneke (2008).

VPC Volume Pair Correction: Each *volume pair* that is cross-correlated to calculate a velocity field has a common calibration model determined by the volume self-calibration applied over the pair of them. This method may be implemented to increase the number of valid particle matches for the self calibration combined with a vibration frequency $\ll 1/\Delta t$. This is the implementation of Michaelis and Wolf (2011).

IVC Individual Volume Correction: Each reconstructed volume has its own calibration model computed by considering each time-step individually in the volume self-calibration. This is the ideal case, each reconstruction is corrected, and suitable for when the vibration frequency is in the order of or greater than $1/\Delta t$.

SVC Single Volume Correction: For each volume pair that is cross-correlated to compute a velocity field, the calibration model is determined by applying the volume self-calibration applied over the first time step of a volume pair only. This implementation could be used where an assumption can be made that the vibration frequency is $\ll 1/\Delta t$.

The volume self-calibration technique is an iterative process, whether applied globally or for individual volume corrections. For these comparisons, the GVC was used as the starting point for the other correction regimes. The GVC obtains the average (or reference) position of all the cameras with respect to the measurement volume. Once the domain of physical volume is known, its dimensions are fixed for the remaining correction regimes. This means that through each iteration of the vibration correction, the cameras move with respect to the volume (figure 9(*a*)).

Figure 9(*b*) shows the evolution of the disparity maps for the IVC case. From the first iteration it is clear that the calibration model is not refined, and owing to the random position of the other cameras, the disparity distribution does not show one strong peak disparity (as would be the case in a non-vibrating experiment, Wieneke 2008), but rather two or three disparity peaks. By the third iteration, the repeated application of the volume-self calibration resulted in disparity maps (hence camera models) that have converged.

Monitoring the disparities d_{ix} and d_{iy} allows for an optimum selection of $\varepsilon_{i,\max}$ to be determined for each iteration. Figure 10(*a*) graphs the root mean square (rms) of the total disparity $d_{\text{rms}} = \sqrt{d_x^2 + d_y^2}$ for each camera against the iteration of the volume self-calibration. In figure 10(*a*), d_{rms} is calculated over all sub-volumes and over 100 images of the first time-step for the IVC method. For the first iteration of the volume self-calibration, $0.3 \leqslant d_{\text{rms}} \leqslant 0.5$ px, which implies that the amplitude of relative vibration for one camera is within the average particle image diameter. As the cameras are vibrating independently of each other, the

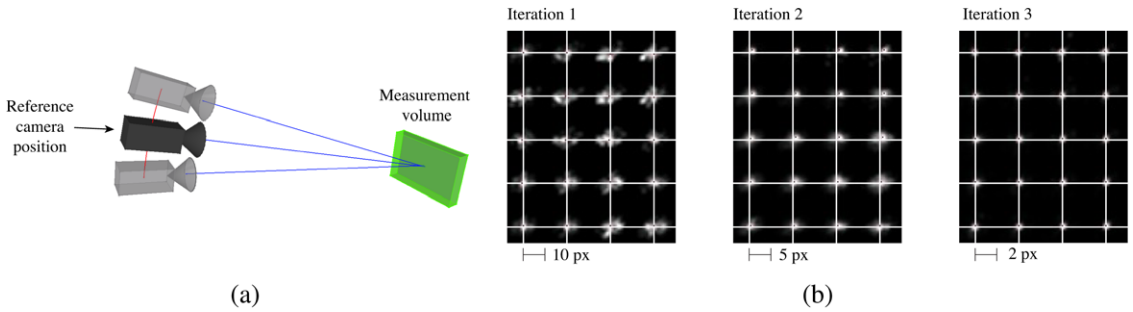

Figure 9. (*a*) Physcial interpretation of vibration correction schemes. (*b*) Sample of disparity maps for the first three iterations of the IVC method.

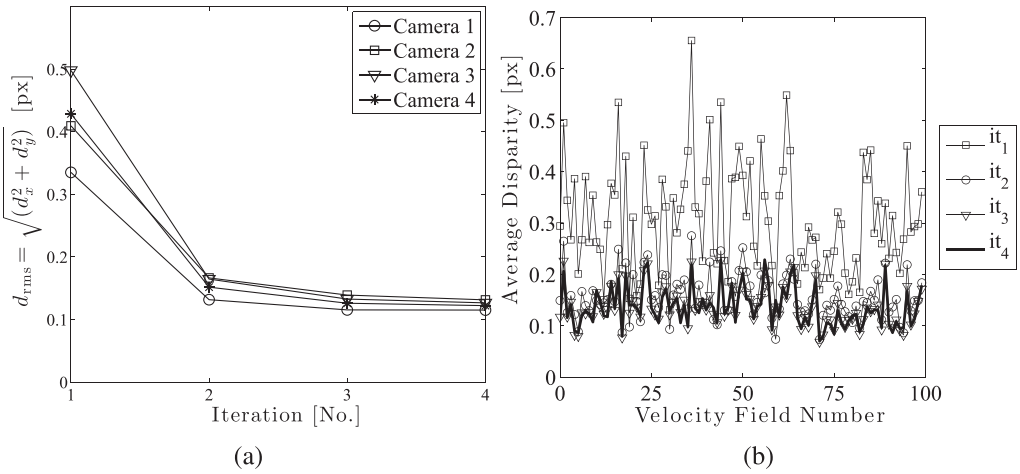

Figure 10. (*a*) Average reduction of ϵ over iterations of volume-self calibration for the IVC case. (*b*) History of average disparities of the entire volume for successive iterations of the volume-self calibration for a sequence of temporally spaced acquisitions.

rms of the total combined disparity is 1 px. As will be seen, this small magnitude of vibration will enable an acceptable reconstruction without vibration correction, however the resulting velocity field and turbulence statistics are more severely affected.

Additionally, a time history of the disparity errors is presented for the IVC case. Figure 10(*b*) shows the average magnitude of the disparities for each time step. A time series analysis like this has the potential to uncover a dominant frequency of vibration. However, in this case, an evaluation of the frequency domain revealed no discernible frequency was obtained.

It was thus found that four iterations of the vibration correction schemes were required, and for the IVC only one iteration was required for the second time-step. It was found that $d_{\mathrm{rms}} \approx 0.2$ px for the second time-step, and was corrected to within an equivalent range as the first time-step after one iteration. This indicates that the frequency of vibration is less than $1/\Delta t$. For each iteration, the $\epsilon_{i,\max}$ was reduced, starting from 10 px for the first iteration and finishing at 2 px for the fourth. In terms of computational effort, one iteration of the IVC/SVC was in the order of 40 s, and one iteration of the VPC was 50 s and thus the SVC case is 20% faster than the IVC and VPC. This time saving may become more significant with larger amplitudes of vibration, however in these experiments the time saved with respect to the reconstruction and cross correlation times was not significant.

5. Experimental results and discussion

5.1. Instantaneous velocity fields

The TPIV analysis gives fully volumetric 3 component and 3 dimensional velocity fields. The vorticity fields ω were calculated to observe and compare the vorticity structures present in each correction scheme (figure 11). In this figure, the vorticity iso-surfaces showing ω_x are plotted with every sixth velocity vector with U_0 subtracted. All of the velocity fields show the same large structures at $255 < x < 275$ mm and $y < 70$ mm. However, as for the smaller structures around the volume, subtle differences can be seen, particularly in the top right hand corner of the figures. Without *a priori* knowledge of the vibration, the GVC case yields acceptable results (figure 11(*a*)).

To enable a direct comparison of the velocity fields obtained from the different correction schemes, the GVC velocity field was subtracted from the three other cases. Figure 12(*a*) shows the first 124 velocity differences for a volume (equivalent to two streamwise rows of dimension *I*). The vibration correction schemes do not modify the same vectors by the same quantity, however in this small sample, the peaks of correction occur at corresponding locations. The magnitude of the corrections in figure 12(*a*) represent up to a maximum of 15% of U_0.

Close observation of these signals reveals that there is some periodicity to these corrections. Figure 12(*b*) shows the frequency domain of the *u* component of the IVC-GVC. The signal

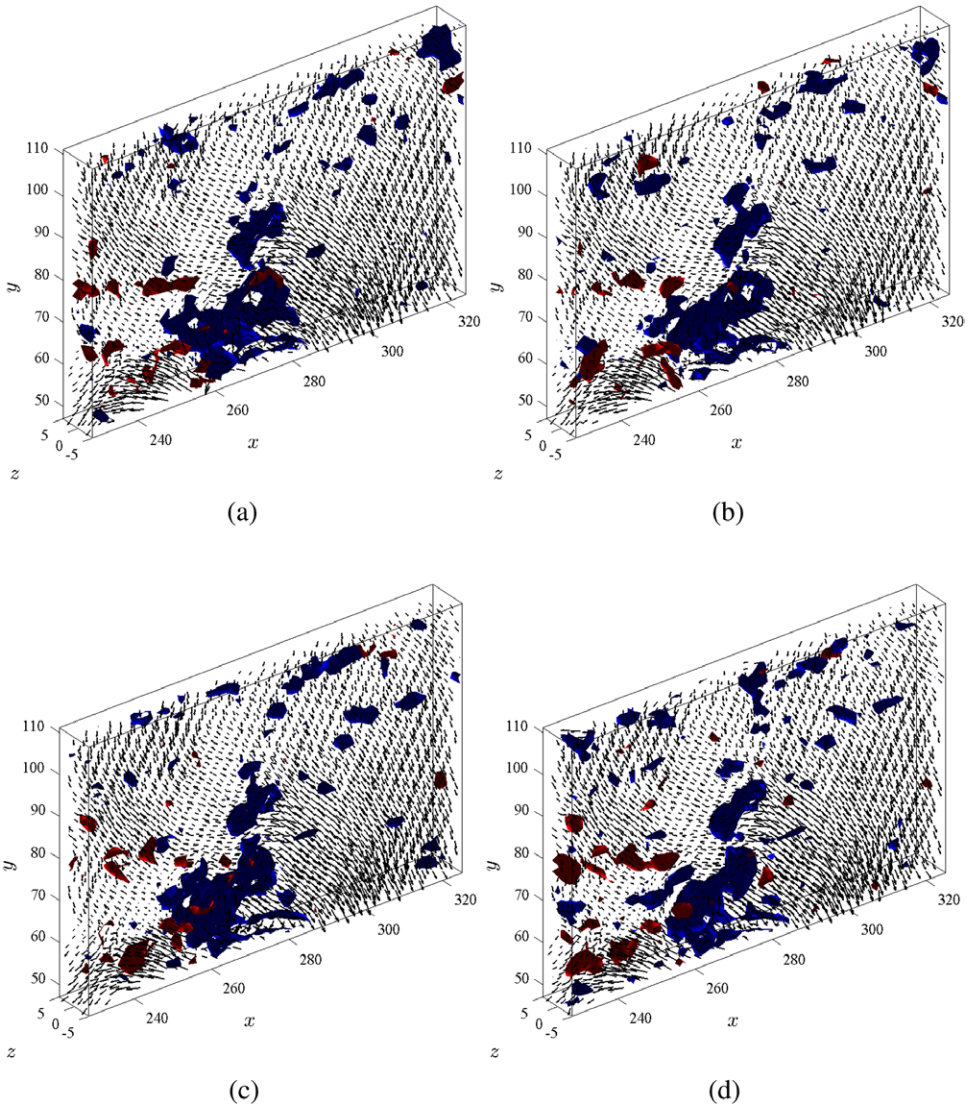

Figure 11. ω_x iso-contours at ± 10 s^{-1} for configuration (*a*) GVC, (*b*) VPC, (*c*) IVC, (*d*) SVC with fluctuating velocity vectors (1/6th plotted for clarity). The flow direction is left to right.

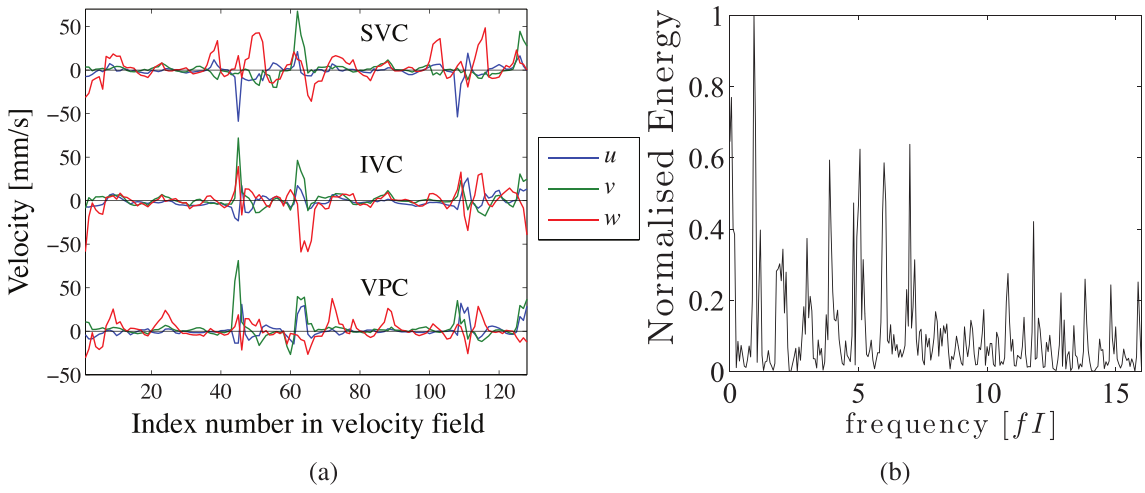

Figure 12. (*a*) Difference between the GVC and the VPC (bottom), IVC (middle) and SVC (top) cases for the first 124 velocity vectors in the volume. (*b*) Frequency domain of the *u* component of velocity for the GVC-IVC case signal.

Table 2. Difference between the GVC and the VPC, IVC and SVC cases, for all velocity fields normalised by the local streamwise velocity component $\overline{u_{GVC}}$.

Case% (c)	std$\left(\frac{u_c - u_{GVC}}{\overline{u_{GVC}}}\right)$(%)	std$\left(\frac{v_c - v_{GVC}}{\overline{u_{GVC}}}\right)$(%)	std$\left(\frac{w_c - w_{GVC}}{\overline{u_{GVC}}}\right)$(%)
VPC	1.32	1.35	2.61
IVC	1.45	1.31	2.64
SVC	1.24	1.36	2.71

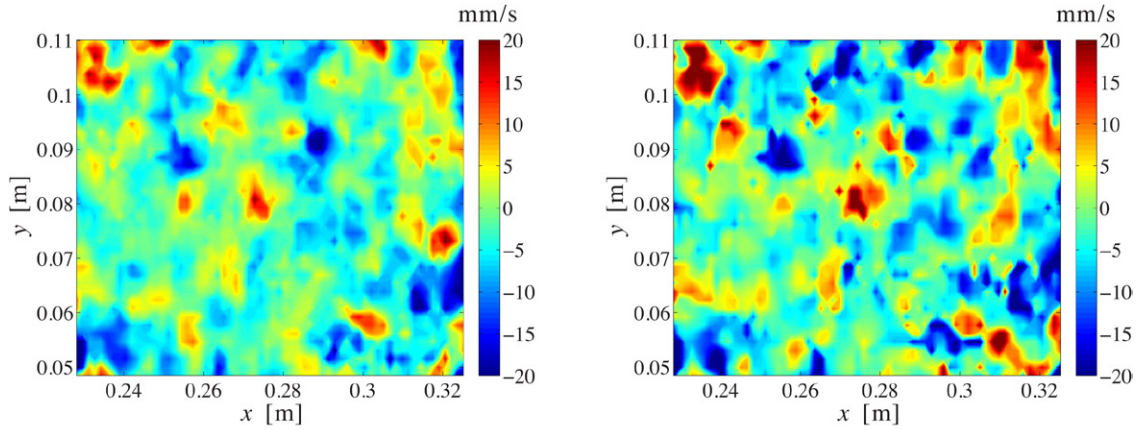

Figure 13. Difference between the GVC and the IVC case for the w component. (a) shows one plane of velocity difference, (b) the sum of the differences along z.

has been normalised so that a frequency of 1 corresponds to one row of velocity vectors I (number of vectors in the x-axis). Figure 12(b) shows that there is a clear dominant frequency of $fI = 1$, which is repeated harmonically along the frequency scale. This will be investigated further in section 6. In the small sample in figure 12(a), there appears to be some other dominating spatial frequencies $< fI = 1$, they are not present in the whole volume.

Table 2 contains the statistics of the difference in velocity fields. Each component of velocity has been normalised by the spatially averaged streamwise velocity U_0 of the velocity field. The modification to the out of plane component w is approximately twice as great as the u and v components. This shows that the velocity field has had significant modification from the GVC, however as the modifications are local, these difference are averaged out when considering the mean or fluctuating components of whole velocity fields. The magnitude of the standard deviation fluctuations in table 2 are between 30–40% of their respective turbulent fluctuation components.

The spatial distribution of the w velocity differences are presented for the IVC case in figure 13. In figure 13(a), one xy-plane of the velocity difference is considered, whereas for figure 13(b), the velocity difference is summed over z. These figures indicate that the vibration correction modifies the velocity field (compared with the GVC case) locally, as opposed to a uniform shift or rotation as may be expected. As the disparity errors are typically less than a particle diameter, the reconstructed particles are in the same location in the reconstructed volume but of different shape or intensity. Thus, the local corrections occur in regions of the volume that have local high or low particle densities.

5.2. Velocity probability density functions

For the four schemes, the normalised velocity probability density functions (PDFs) were calculated (figure 14). The PDFs reveal that the w component of the velocity for the GVC case (figure 14(a)) contains a higher peak at the normalised velocity of −0.5. On the other hand, there is no significant difference to the u and v components of velocity. This result is supported by the statistics presented in table 2, where the majority of the modifications were on the w component. The PDFs reveal that this modification of w was a local distribution, however globally the range and statistics of the variable were largely unmodified. To ensure that the peaks in the PDFs were not due to peak-locking, these plots were presented in terms of voxel displacement. It was observed that there was no peak-locking effect, meaning that the peaks in the PDFs are flow features.

5.3. Reconstruction quality

The reconstruction quality, denoted by the correlation coefficient Q_I (equation (4)) as proposed by Elsinga *et al* (2006), is one indicator of the quality of the reconstruction. Q_I is a measure of the difference between the intensity of the pixels (i, j) of the filtered images I and the intensity of the corresponding pixel locations, I_r, by projecting the reconstructed volume intensity. A widely accepted threshold for reconstruction quality is 75% .

$$Q_I = \frac{\sum I(i,j) \cdot \sum I_r(i,j)}{\sqrt{\sum I^2(i,j) \cdot \sum I_r^2(i,j)}} \tag{4}$$

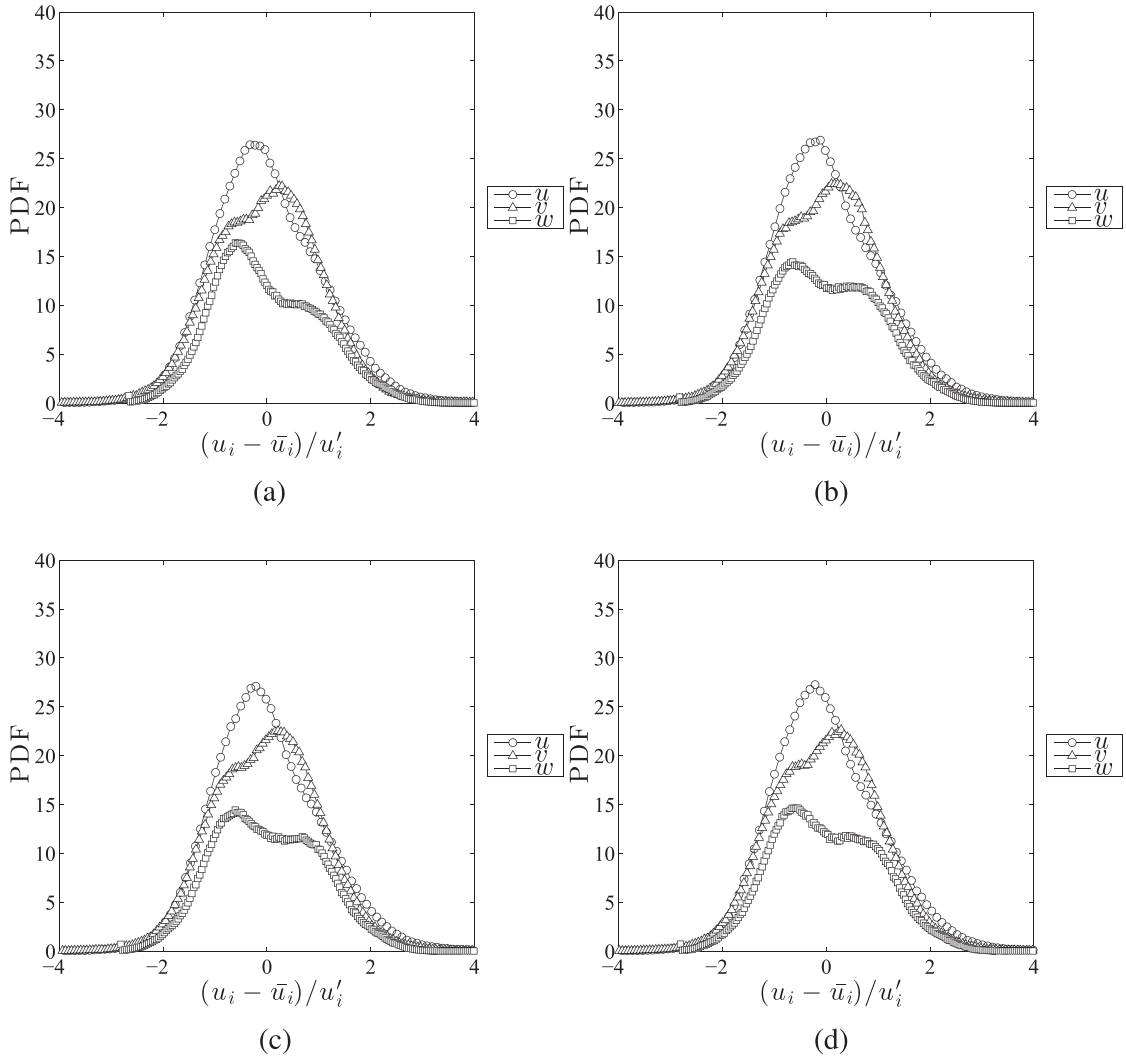

Figure 14. Normalised PDFs of the velocity components (*a*) GVC, (*b*) VPC, (*c*) IVC, (*d*) SVC.

Table 3. Average reconstruction quality coefficient Q_I for t_0 and t_1, mean and rms of the SNR, percentage of spurious vectors and the mean and rms of the velocity field divergence for each of the vibration correction regimes.

Correction	$\overline{Q_I}\,(t_0)\,(\%)$	$\overline{Q_I}\,(t_1)\,(\%)$	$\overline{\mathrm{SNR}}$	$\overline{\mathrm{MF}}\,(\%)$	$\overline{\nabla\cdot\mathbf{u}}\ (\mathrm{s}^{-1})$	$\nabla\cdot\mathbf{u}'\ (\mathrm{s}^{-1})$
GVC	80.0	80.5	3.21	1.49	0.10	5.52
VPC	80.3	80.8	3.22	1.43	0.15	5.51
IVC	80.1	80.1	3.23	1.45	0.09	5.77
SVC	79.1	80.0	3.21	1.48	0.13	5.61

The average results of the reconstruction quality over 100 volumes are presented in table 3, grouped in time steps. The average Q_I for both time steps and for all correction regimes are found to be equivalent. Another indication of reconstruction quality is found by examining the laser sheet profiles as shown in figure 15, where the reconstructed fields have been trimmed to size. The laser sheet profiles are computed by summing the intensities of all *xy*-planes of voxels in a reconstructed volume. For the first time step t_0, figure 15(*a*) shows that in this particular volume the laser sheet profiles are equivalent. In the second time-step t_1 (figure 15(*b*)), the IVC case has produced a higher intensity laser sheet profile, the GVC and VPC schemes have laser sheet profiles not too dissimilar to t_0 and the SVC scheme, which has used the camera model from t_0, has generated a weaker signal. This change in signal has been shown to be due to the misalignment of the camera models (see figure 18).

5.4. Correlation quality and divergence

The averaged signal-to-noise ratio (SNR) of the cross-correlation was computed to investigate its effect on the correction on the velocity (table 3). The SNR is defined as the ratio between the peak (cross-correlation signal maximum)

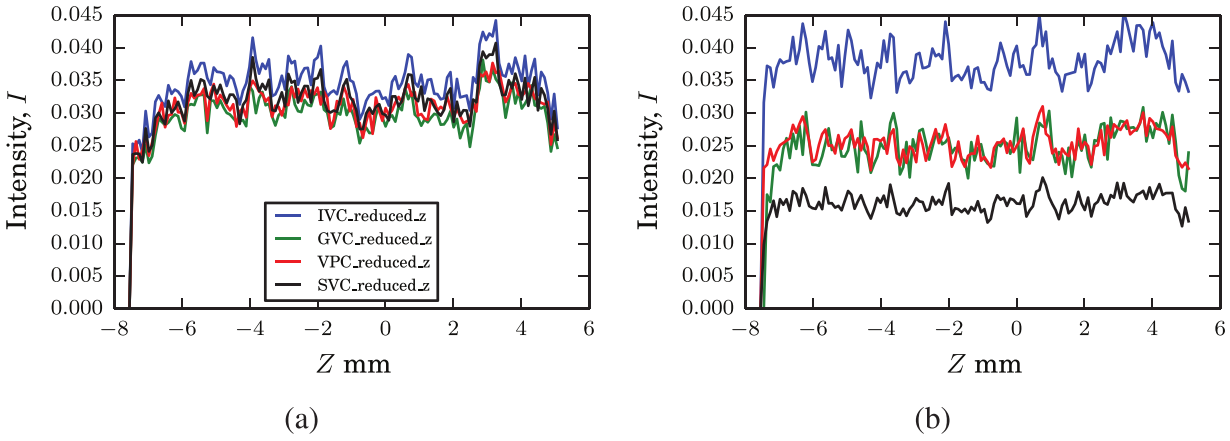

Figure 15. Laser sheet profiles of a single reconstructed volume for (*a*) t_0 and (*b*) t_1.

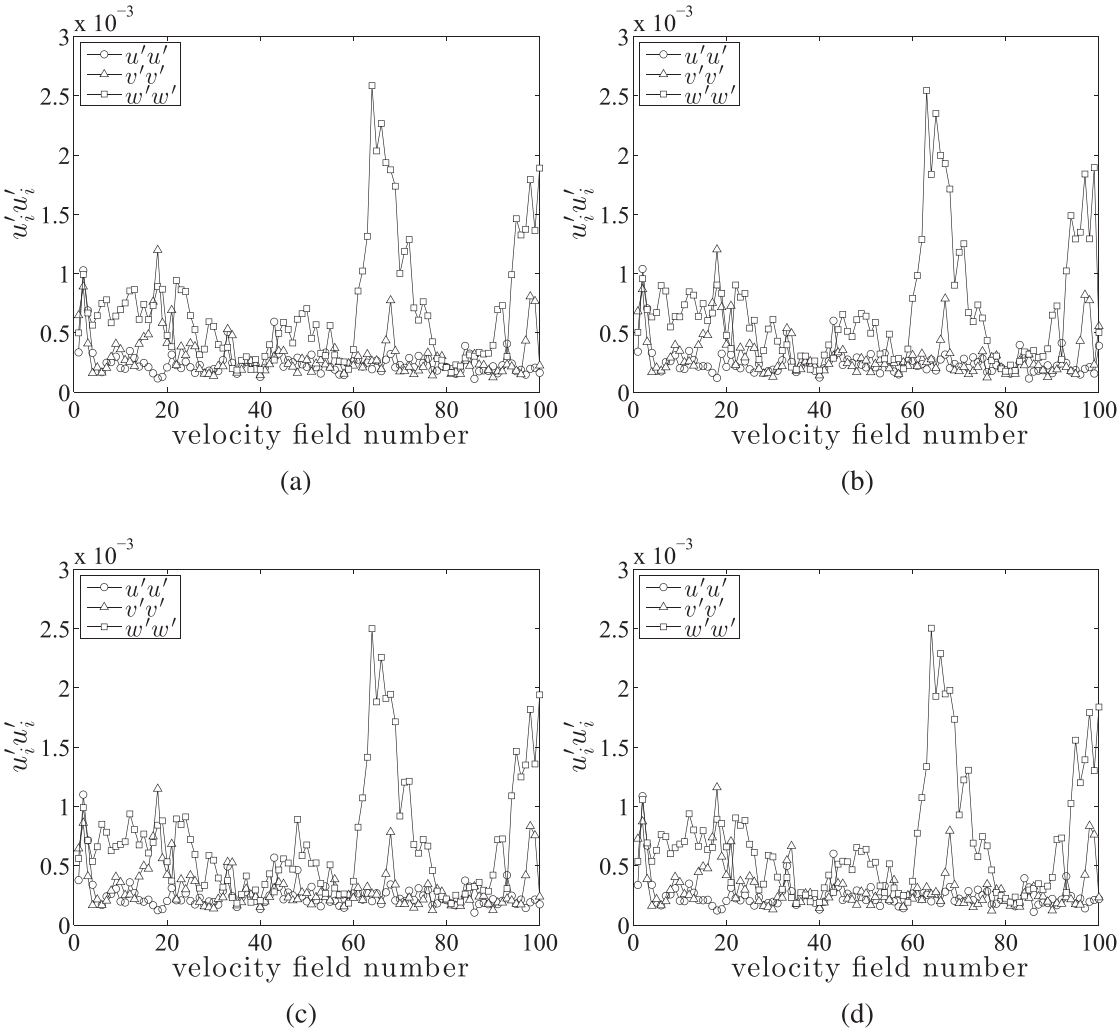

Figure 16. Evolution of components of turbulent kinetic energy against time for (*a*) GVC, (*b*) VPC, (*c*) IVC, (*d*) SVC.

and the second highest local peak in the signal. The local peaks are found by considering the immediate 26 neighbours of the centre of a 3 × 3 × 3 sliding box. For all correction cases, the SNR of the cross-correlation is equivalent. The mean number of spurious vectors $\overline{\mathrm{MF}}$, as computed by the universal median filter (Westerweel and Scarano 2005), is likewise presented in table 3. Again, no significant difference is observed between the number of corrected vectors.

Finally, the effect of the correction regimes on the divergence of the velocity field was examined and is presented in

Table 4. The root mean square of the components of and total vorticity, ω (s^{-1}).

Correction	$\langle\omega\rangle$	ω'_x	ω'_y	ω'_z
GVC	6.57	4.30	4.38	4.30
VPC	6.47	4.22	4.34	4.18
IVC	6.46	4.22	4.34	4.16
SVC	6.47	4.25	4.34	4.19

the same table. The spatio-temporal mean (denoted with an over-bar) and standard deviation (denoted with a prime) are presented in table 3. For an incompressible flow, such as the flow measured in this article, the divergence $\nabla\cdot\mathbf{u} = 0$. Although this measure is only valid for infinitesimal fluid elements (that is measurement resolution at the Kolmogorov scales), for a given resolution, a greater departure from zero divergence can indicate greater random measurement errors. As the velocity vectors are not independently sampled, these metrics are displayed to show what is commonly adopted practice in the literature rather than a rigorous uncertainty analysis for these measurements. All vibration correction schemes returned similar divergence statistics. Thus, from these criteria that are commonly used to validate the quality of TPIV experiments, one could be lead to the conclusion that all of the velocity fields are equivalent.

5.5. Vorticity

Table 4 shows the mean total vorticity $\langle\omega\rangle$ and the rms of each of its components denoted with a prime. The vorticity is calculated as per equation (5), where the gradients were calculated by a second order central difference scheme, and the magnitude computed from the Euclidean norm of all components. The three vibration correction cases have a similar effect on the vorticity, that is to reduce the magnitude of its components. The effect of the local modifications to the velocity field are seen to have a greater effect on the deforming gradients as opposed to the normal gradients of the divergence criteria. Thus in terms of the vorticity, the vibration correction cases have modified the vorticity data on average by a similar magnitude.

$$\omega = \|\nabla \times \mathbf{u}\| \qquad \text{where } \mathbf{u} = (u, v, w) \tag{5}$$

5.6. Turbulence kinetic energy

The turbulence kinetic energy k, is a measure of the energy of the fluctuating components of velocity. For 3C–3D velocity field data, k is defined as

$$k = \frac{1}{2}\left(\overline{(u'\cdot u')} + \overline{(v'\cdot v')} + \overline{(w'\cdot w')}\right) \tag{6}$$

where u', v', w' are the respective x, y, z fluctuating components of velocity. A comparison of k and its components is presented in table 5. The IVC case has a slightly higher k than the other corrected cases. The larges components contributing to k for the three vibration correction schemes are a result of the z components, w'. It is well documented that

Table 5. Turbulence kinetic energy and components, k ($mm^2\ s^{-2}$) and energy dissipation ε ($mm^2\ s^{-3}$). Comparison between the vibration correction schemes and the 2D PIV results (where possible).

Correction	k	$u'\cdot u'$	$v'\cdot v'$	$w'\cdot w'$	$\langle\varepsilon\rangle$	ε_{rms}
GVC	625	247	308	694	1290	2410
VPC	625	250	308	692	1320	3090
IVC	635	250	307	713	1180	1990
SVC	625	246	308	696	1320	3300

TPIV reconstruction can induce a bias in the direction of the thickness of the laser sheet through the reconstruction of elongated particles (Scarano 2013). The elongated particles lead to broadened correlation peaks in the z direction. The performance of three point interpolation schemes on the correlation peak to find sub-voxel displacements loses precision and hence affects the magnitude $w'\cdot w'$. To verify if the higher energy in the w' direction is due to this effect, the evolution of the components of turbulent kinetic energy are plotted against the corresponding velocity field number figure 16. Large peaks in the $w'\ w'$ component are observed between time-step 60 and 80 for all of the cases. There is no similar peak in the mean disparity values (figure 10) that may point to a moment of high amplitude vibration, and thus this elevated $w'\cdot w'$ is a flow event. As the acquisition rate of a velocity field is 5 Hz, this peak of kinetic energy appears to have occurred over approximately 4 s. Over a short measurement sample such as this, the event has elevated this out of plane component.

5.7. Energy dissipation

The energy dissipation $\langle\varepsilon\rangle$ was obtained directly from equation (7) (George and Hussien 1991) from the TPIV measurements:

$$\begin{aligned}\langle\varepsilon\rangle \;=\; \nu\Bigg\{ & 2\left(\left\langle\frac{\partial u}{\partial y}\frac{\partial v}{\partial x}\right\rangle + \left\langle\frac{\partial u}{\partial z}\frac{\partial w}{\partial x}\right\rangle + \left\langle\frac{\partial v}{\partial z}\frac{\partial w}{\partial y}\right\rangle\right) \\ & + \left\langle\left(\frac{\partial u}{\partial y}\right)^2\right\rangle + \left\langle\left(\frac{\partial v}{\partial x}\right)^2\right\rangle + \left\langle\left(\frac{\partial u}{\partial z}\right)^2\right\rangle \\ & + \left\langle\left(\frac{\partial w}{\partial x}\right)^2\right\rangle + \left\langle\left(\frac{\partial v}{\partial z}\right)^2\right\rangle + \left\langle\left(\frac{\partial w}{\partial y}\right)^2\right\rangle \\ & + 2\left(\left\langle\left(\frac{\partial u}{\partial x}\right)^2\right\rangle + \left\langle\left(\frac{\partial v}{\partial y}\right)^2\right\rangle + \left\langle\left(\frac{\partial w}{\partial z}\right)^2\right\rangle\right)\Bigg\}\end{aligned} \tag{7}$$

For the appropriate use of the ensemble average, the flow must be fully developed, that is $\partial\epsilon/\partial t = 0$. Although the spatial resolution of the TPIV measurements do not capture the Kolmogorov scale, the energy dissipation is calculated to obtain understanding of its magnitude in the larger scales, those that may have greater impact on the swimming capabilities of fish. The lack of adequate resolution in these measurements means that the energy dissipation signal is dominated by noise (as shown by Worth *et al* 2010). As such, the raw values obtained in this section cannot be taken to be the correct magnitude of the large-scale dissipation, and a comparison with higher resolution measurements are required. However, these calculations can give an indication as to the

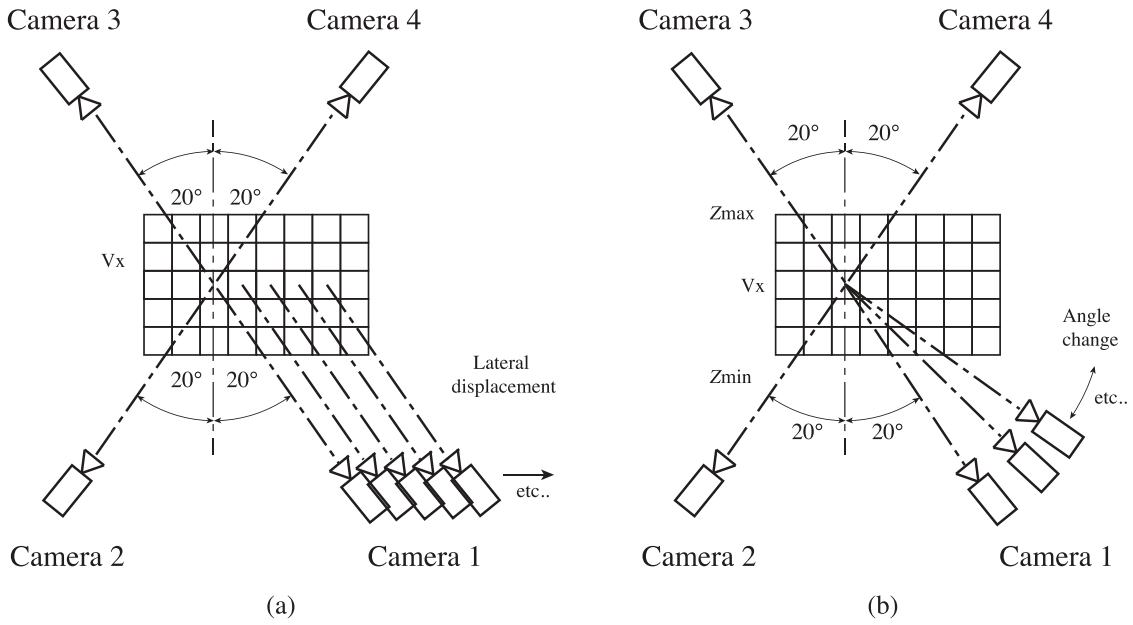

Figure 17. Schematic of vibration implementation (*a*) Single camera translation (*b*) Single camera rotation

Table 6. Key parameters of synthetic TPIV model to simulate vibration.

Parameter	Description
Camera arrangement	4 cameras, inverted pyramid, 20° declination and subtended angle
Image size	All cameras: 512 × 512 px with no noise (perfect filtering), $N_s = 0.6$
d_τ	$\mathrm{d}\tau \approx 5.4$
TPIV algorithm	BiMart 3 iterations, $\mathscr{B} = 4$, identical to experimental implementation
Volume size (I:J:K)	512 : 512 : 128 vx
IV size	64 × 64 × 64
IV overlap	50%
Vector field dimensions	15 × 15 × 3
(max, rms) particle displacement	(±5 vx, 1.5 vx)
Spatial resolution	7.5η

effect of the vibration correction schemes on the calculation of higher order turbulence statistics. Following this, the mean and rms of ϵ are presented in table 5. As seen in equation (7), the calculation of the energy dissipation relies on a combination of the sum of the product of all nine velocity gradients in the velocity gradient tensor. As a result, random noise in the velocity fields would be amplified, potentially dominating the signal. Table 5 shows the ensemble average and the rms of ϵ. In this case, the IVC scene has the lowest rms by ≈50%, indicating that particularly for higher order turbulence analyses, the correction of TPIV results with an IVC scheme is necessary to reduce the noise in the velocity data. The effect of vibration on turbulence statistics is investigated further in section 6.5.

6. Synthetic model to study camera vibration

6.1. Implementation

In order to further investigate the results presented in section 5, a synthetic model was implemented to closely resemble the experimental conditions. A single realisation of a direct numerical simulation (DNS) velocity field was seeded with particles that were used to generate synthetic TPIV images, of which it was possible to extract four independent velocity fields. The synthetic image generator used was the same as that described in Thomas *et al* (2014); the key input parameters for this investigation are contained in table 6. Further details of the simulated homogeneous isotropic turbulence velocity field can be found in Lecordier *et al* (2001).

The vibration of a four camera system is complex, with combinations of independent and dependent camera translations and rotations of varying magnitudes and frequencies. The main effect of vibration on the tomographic reconstruction, regardless of complexity, is to cause a misalignment of the lines-of-sights of corresponding particle images. Thus, the aim of this section is to investigate the effects of camera vibration, or misalignment, in the simplest possible manner to fully describe the observations in the experimental results. Additionally, using a 'perfect' simulation allows the analysis to be free from contamination of experimental noise sources, such as non-uniform particle size, inhomogeneous illumination and optical aberrations. To this end, a systematic translation along the x-axis, and independently, a systematic rotation

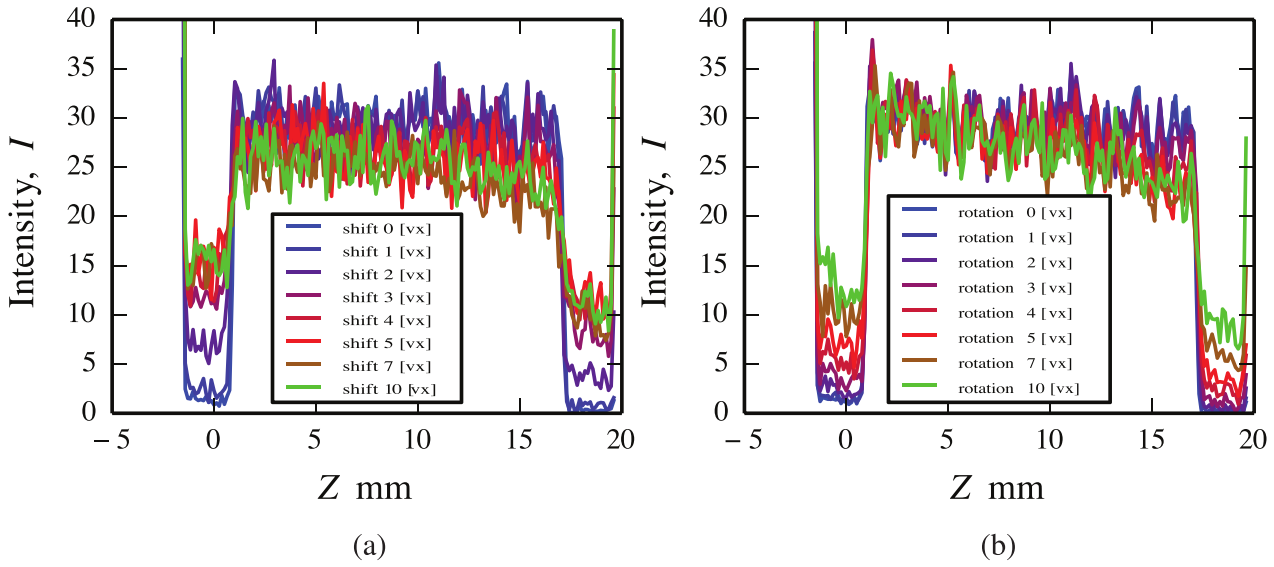

Figure 18. Laser sheet profiles for the synthetic case comparing the intensity on the camera model shift. (*a*) Shift, (*b*) rotation.

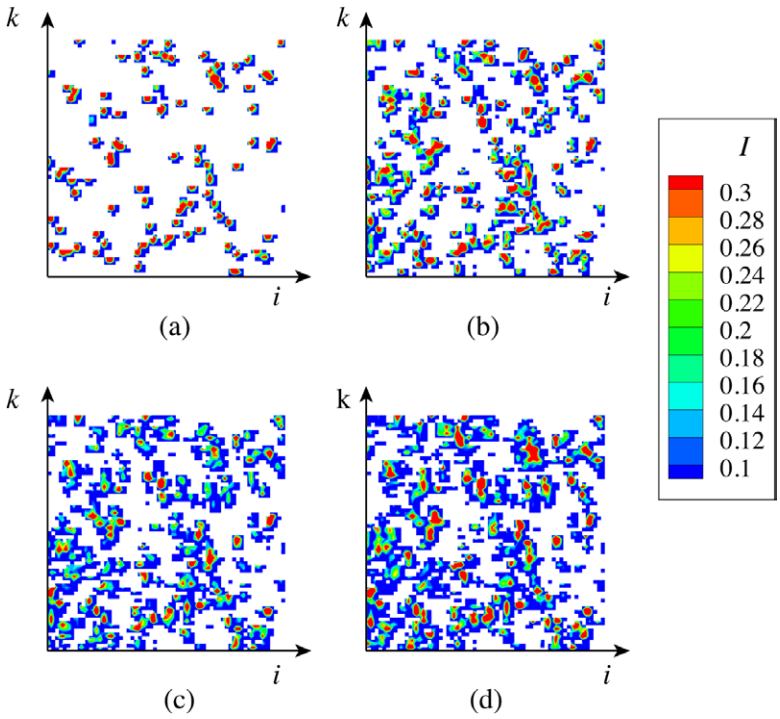

Figure 19. 2D projections of reconstructed volume in a 64 × 64 × 64 window at (*a*) 0 error, (*b*) 2 vx shift, (*c*) 5 vx shift, (*d*) 10 vx shift.

about the *y*-axis was applied to one camera in the model (figure 17). For the translation, an increasing displacement of 1 vx increments was applied, while for the rotation, an additional angle was applied so that the line of sight of the camera had a 1 vx shift at the outer edges of the volume. For brevity, the remainder of this section will refer to this type of rotation as a rotation by a certain number of voxels.

6.2. Reconstruction and cross-correlation metrics

This section describes the effect that the translation and rotation of one camera has on tomographic reconstruction and cross-correlation metrics. Figure 18 shows the effect of the shift and rotation on the laser sheet profile. In both cases, an increase in camera misalignment results in a reduction in a significant reduction in signal quality. Additionally, the rotation case introduces a dissymmetry, where the side of the laser sheet profile that the rotated camera is positioned (positive *Z*) has between 20% to 30% less intensity than the opposite side of the volume. The SNR of the reconstruction (from Scarano (2013)) at 0 vx misalignment is approximately 30 and at 10 vx misalignment between 2 and 3.

Figure 19 shows the effect of the translation misalignment on the reconstructed particles of a single interrogation volume

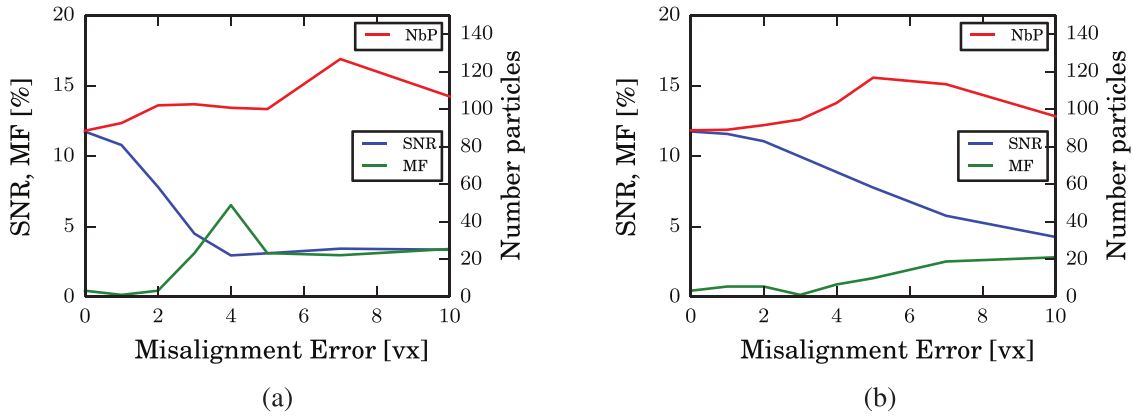

Figure 20. Effect of camera error on the average SNR (%), MFF (%) and NbP, equivalent to number of particles, per IW. (*a*) shows the effect of translations, (*b*) for rotations.

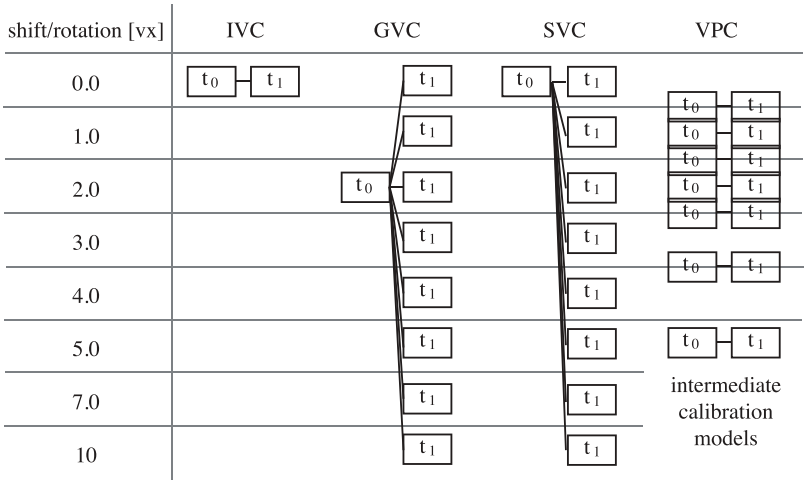

Figure 21. Schematic representation of the synthetically created vibration implementation schemes.

(IV) located in the centre of the volume. The IV intensities have been projected onto one face to produce these two-dimensional images. Figure 19(*a*) shows the intensities at 0 vx error, (*b*) at 2 vx shift, (*c*) at 5 vx shift and (*d*) at 10 vx shift. As the misalignment error increases, it can be seen that ghost particle production increases dramatically, until the projected image is dominated by intensities that are not present in the perfectly aligned case.

Figure 20 shows the effect of the translation misalignment (figure 20(*a*)) and rotation (figure 20(*b*)) on the cross-correlation SNR, number of local peaks per IV (NbP) and vector outlier detection by median filter flags (MFF). NbP is determined by calculating the number of local peaks in the IV, which corresponds to the number of reconstructed particles, ghosts or otherwise. Regarding the translation errors, the SNR decreases rapidly until hitting a plateau at a translation approximately equal to d_τ. The MFF peaks at the same level of translation. NbP tends to increase beyond a translation error of d_τ, and tapers off beyond this error. This metric would be sensitive to N_s and d_τ, however the full parametrisation of these variables is beyond the scope of this study. The rotation errors yield similar trends, albeit more gradually. This is due to the lines-of-sight of all cameras remaining error free in the central plane of the reconstruction domain.

6.3. Simulation of vibration correction schemes

The vibration correction schemes used for the experiment (section 4.1) were recreated in the synthetic model. Figure 21 shows a schematic of how the translation and rotation errors were combined to replicate the experimental conditions. The schematic shows the number of permutations tested for each correction scheme. The assumptions used for each case are outlined as follows:

IVC The correct implementation of the IVC scheme retrieves the correct camera models for both time steps, t_0 and t_1. Therefore, in the synthetic model, the IVC case has perfect camera models.

GVC It is highly improbable that t_0 has no calibration error for a GVC, therefore t_0 is assumed to have a misalignment of 2 vx. Then, t_1 is varied through the set of misalignment errors. SVC t_0 is perfectly corrected (like the IVC), and

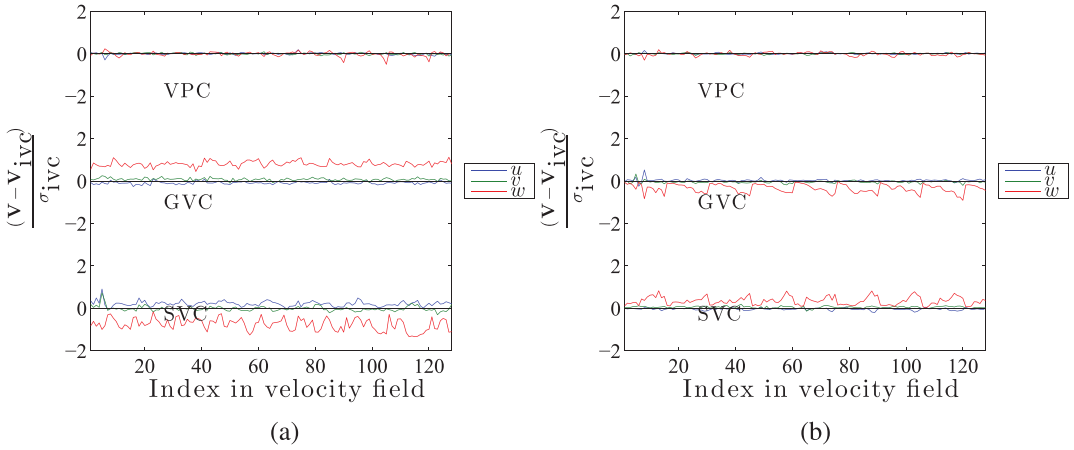

Figure 22. Difference between velocity fields, normalised by the standard deviation σ of the velocity of the IVC case: (*a*) 1 vx translation, (*b*) 1 vx rotation.

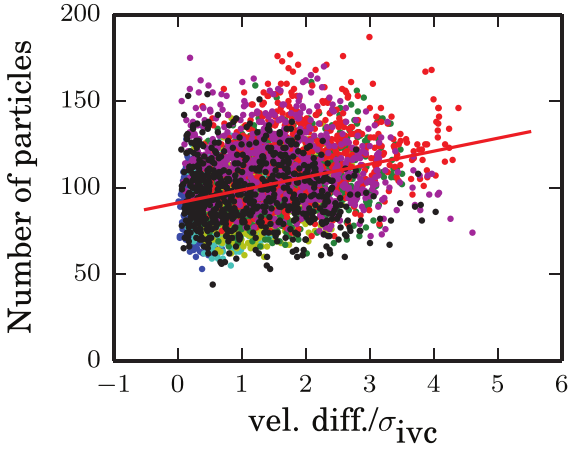

Figure 23. Scatter plot of the number of detected particles in an IV and the magnitude of local velocity correction in the GVC. The velocity has been normalised by the standard deviation σ of the IVC scheme. The colour of the markers represents a level of misalignment. There is a weak correlation ($R^2 = 0.2$) between number of particles within an IV and the size of the velocity correction.

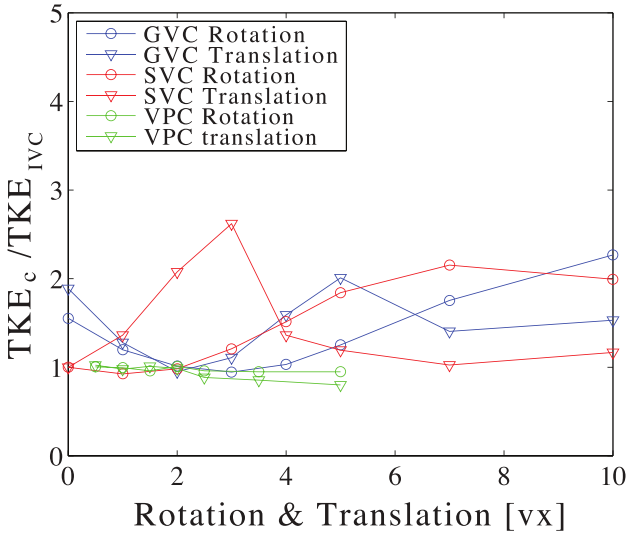

Figure 24. Evolution of the turbulent kinetic energy (TKE) for each correction case *c*, normalised by the IVC case, with respect to increasing misalignment error.

then similar to the GVC, the second time step t_1 has a varying level of error.

VPC For misalignments not significantly greater than d_τ, disparity maps would not necessarily show two separate peaks. The resulting camera model would then be the average of perfect calibration and misalignment error.

As the IVC case only has one permutation, the several results in this section will be normalised by this case. It also represents the best possible reconstruction quality for this particular arrangement. This normalisation permits an analysis of the simulated effect of increasing vibration as the misalignment increase.

6.4. Correction schemes and their effect on velocity

Figure 22 shows the differences to local velocity field for each camera model, normalised by the standard deviation of the IVC case, σ_{ivc}. The translation error yields very similar results to the experimental results, where the velocity field is shown to be updated locally. A notable difference is the clear shift of velocity components that is not observed in the experimental results. This is believed to be an artefact of moving only one camera in the synthetic case, as opposed to all cameras vibrating in the experimental case. The rotation error also modifies the velocity field locally, however rather than randomly, the velocity correction has a dominate frequency at I vectors to the velocity field, which is particularly evident in the GVC and SVC case. This result provides evidence to suggest that the periodicity reported in the experimental case (figure 12) is due to rotation errors in the calibration models.

A hypothesis made in section 5 was that this local correction could be due to local particle distributions. Figure 23 plots the number of particles, again approximated by the number of local intensity peaks in an IV, compared to the magnitude of

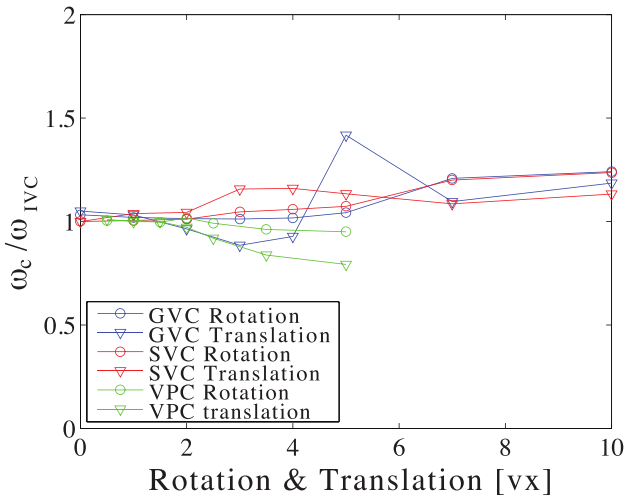

Figure 25. Evolution of the magnitude of vorticity ω for each correction case c, normalised by the IVC case, with respect to increasing misalignment error.

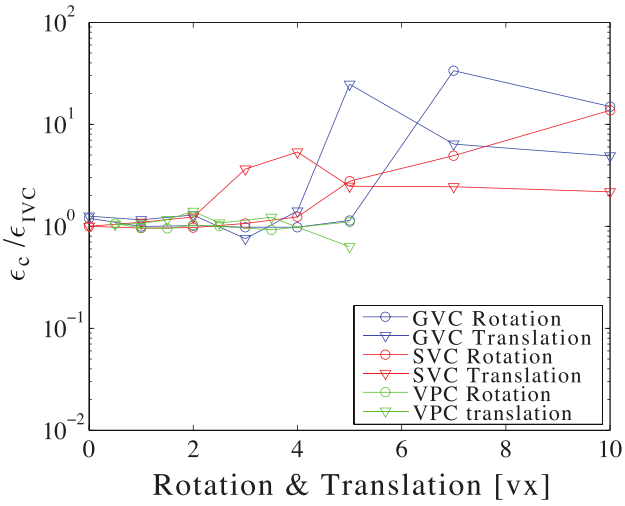

Figure 26. Evolution of the energy dissipation ϵ for each correction case c, normalised by the IVC case, with respect to increasing misalignment error.

velocity difference chance, normalised by σ_{ivc}. The colours of the scatter markers indicate a different misalignment error. Despite three cameras maintaining perfect calibration, there is a weak trend that lends weight to support this hypothesis.

6.5. Correction schemes and their effect on turbulence statistics

Figure 24 shows the evolution of TKE function of the misalignment error. The GVC case has an initial error owing to the 2 vx error imposed on its t_0 reconstructed volume. Interestingly, the magnitude of TKE for the GVC case approaches the IVC level when its t_1 volume also has a 2 vx misalignment. The SVC correction case augments significantly within d_τ, after which its level drop off. For larger errors, the rotation errors are more significant for both the GVC and SVC case. The VPC case remains relatively constant, and its magnitude of TKE actually decreases to approximately 90% of the IVC case. These results indicate that the noise induced by the misalignment errors can significantly effect the TKE statistics, particularly the SVC and GVC cases. As VPC has identical error on both time steps, the ghost particles have the same relative motion and position in both time steps and act to smooth the velocity field and hence TKE, a result also reported by Elsinga *et al* (2010).

Figure 25 shows the evolution of the vorticity magnitude ω as it evolves as a function of the misalignment error. Similar to the TKE analysis, the VPC acts to smooth the velocity field and likewise ω. This is indeed the observation for the GVC case when the misalignment errors on t_1 are ± 1 vx of t_0. The GVC exhibits a maximum at the particle image diameter, and for larger errors appears to plate at 15% greater than the IVC vorticity magnitude. This figure shows that there can be a 20% fluctuation in ω magnitude averaged for the entire velocity field.

Figure 26 shows the evolution of the energy dissipation ϵ as a function of the misalignment error. Note that in this figure has a log scale on the ordinate axis of the graph. As ϵ is computed by a large combination of all velocity gradients in the velocity gradient tensor (equation (7)) can increase by an order of magnitude after approximately one particle diameter of shift/rotation. This result is of particular importance for experiments that wish to resolve the kolmogorov scale to calculate ϵ, that essentially undetectable vibrations within a particle diameter can cause significant errors on the calculation. For vibrations larger than d_τ, the GVC and SVC case exceed the IVC value by greater than an order of magnitude.

7. Conclusion

This paper investigated and quantified the effect of vibration on experimental tomographic particle image velocimetry (TPIV) measurements in a turbulent open channel flow. Open channel measurements can be challenging due to the irregular free surface that scatters the laser sheet, bubble entrainment, and vibration. Four cameras were positioned so that they all observed the forward scatter from the particles and the use of prisms was not employed to allow full optical access to the pool. To offset the effect of vibration on the measurements, three vibration correction regimes, namely the Volume Pair Correction (VPC), Individual Volume Correction (IVC), and Single Volume Correction (SVC) were implemented and compared to a Global Volume Correction (GVC), a standard implementation of the volume self-calibration (Wieneke 2008).

In this case, where the vibration is within a particle diameter, it is shown that several criteria that are typically used to determine the quality of the reconstructed particle volume, such as the Q_I correlation coefficient and the laser sheet profiles, could be misleading. It was shown that the vibration correction schemes converged to velocity field specific camera models, the ideal IVC case correcting each particle time step, compared to the GVC case which is considered to be the standard application. We therefore recommend that vibration, or lack thereof, should be verified, even if the commonly used metrics indicate good reconstruction quality. These findings were confirmed by the implementation of a synthetic model. The incremental

translation and rotation of a single camera was able to explain and quantify the behaviour and camera model misalignments between two time steps caused by vibrations.

The correction schemes are shown to modify the velocity field locally, a result that can be easily hidden when taking statistics over a whole velocity field or set of velocity fields. Significant differences between the correction models and the GVC case were in particular the vorticity calculations and the calculation of higher order turbulence variables such as the energy dissipation. This result in particular was confirmed in the synthetic case. The optimal choice of correction scheme depends on a compromise between the number of particles available to correct the camera model, and the amplitude and frequency of vibration compared to Δt. The IVC scheme is ideal, correcting each time step. Particularly for amplitudes of vibration larger than the particle image diameter, only the IVC scheme can properly correct the reconstruction correctly. If particle seeding is too low however, and providing that the vibration amplitude is also less than a particle image diameter, the IPC scheme could be employed. For low frequency vibrations, the SVC scheme reduces computational effort, however for the self-calibration implementation used in this work, the computational savings are insignificant compared to the reconstruction and cross-correlation calculations. According to the synthetic model, the SVC scheme was the most sensitive to vibration errors, and therefore its use is strongly discouraged.

This work has implications for experimental measurements where vibrations are unavoidable and seemingly undetectable, particularly in high flow rate open channel flows. It has been shown that for a relatively small amount of computational effort, the IVC can correctly modify the camera models for each time step. Likewise, a simple synthetic model was implemented that could explain the effect on vibration on reconstruction and cross-correlation metrics as well as turbulence statistics. The perspectives of this work are to fully analyse the features of the flow to be applied to fish measurements. Additionally, the application of this type of analysis where local corrections in the measurement volume are necessary, such as in flows with local refractive index changes, will be investigated.

Acknowledgments

The first author would like to express gratitude for the Australian Postgraduate Award (APA), J McConnell scholarship from the University of Sydney, and a research grant from the University of Poitiers. The experiments were conducted at the University of Poitiers, France, and were funded by the ANR VIVE3D, the FEDER and the AFDAR project for the development of TPIV. Many thanks to Dr Bertrand Lecordier for providing us with the DNS velocity field data.

References

Atkinson C H and Soria J 2009 An efficient simultaneous reconstruction technique for tomographic particle image velocimetry *Exp. Fluids* **47** 553–68

Byrne C 2009 Block-iterative algorithms *Int. Trans. Oper. Res.* **16** 427–63

Calluaud D, Pineau G, Texier A and David L 2014 Modification of a vertical slot fishway with a supplementary cylinder *J. Hydraul. Res.* **52** 614–29

DeSilva C M, Baidya R, Khashehchi M and Marusic I 2011 Assessment of tomographic PIV in wall-bounded turbulence using direct numerical simulation data *Exp. Fluids* **52** 425–40

Discetti S and Astarita T 2011 A fast multi-resolution approach to tomographic PIV *Exp. Fluids* **52** 765–77

Discetti S, Astarita T, Industriale I, Aerospazio S and Federico N 2013 Stability of single image self-calibration for tomographic PIV *10th Int. Symp. on Particle Image Velocimetry* (*Delft, The Netherlands, 1–3 July 2013*)

Elsinga G E, Scarano F, Wieneke B and Oudheusden B W 2006 Tomographic particle image velocimetry *Exp. Fluids* **41** 933–47

Elsinga G E, Westerweel J, Scarano F and Novara M 2010 On the velocity of ghost particles and the bias errors in Tomographic-PIV *Exp. Fluids* **50** 825–38

George W and Hussien H 1991 Locally axisymmetric turbulence *J. Fluid Mech.* **233** 1–23

Lacey J, Neary V, Liao J, Enders J and Tritico H 2012 The IPOS framework: linking fish swimming performance in altered flows from laboratory experiments to rivers *River Res. Appl.* **28** 429–43

Lecordier B, Demare D, Vervisch L M, Reveillon J and Trinite M 2001 Estimation of the accuracy of PIV treatments for turbulent flow studies by direct numerical simulation of multi-phase flow *Meas. Sci. Technol.* **12** 1382–91

Maas H G, Gruen A and Papantoniou D 1993 Experiments in fluids particle tracking velocimetry in three-dimensional flows *Exp. Fluids* **15** 133–46

Michaelis D and Wolf C C 2011 Vibration compensation for tomographic PIV using single image volume self calibration *9th Int. Symp. on Particle Image Velocimetry* (*Kobe, Japan, 21–23 July 2011*) vol 2

Putze T and Maas H G 2008 3D determination of very dense particle velocity fields by tomographic reconstruction from four camera views and voxel space tracking *Int. Arch. Photogram. Remote Sensing Spatial Inform. Sci.* **37** (B5) 33–8

Scarano F 2013 Tomographic PIV: principles and practice *Meas. Sci. Technol.* **24** 012001

Tanaka T and Eaton J K 2007 A correction method for measuring turbulence kinetic energy dissipation rate by PIV *Exp. Fluids* **42** 893–902

Thomas L, Tremblais B and David L 2014 Optimization of the volume reconstruction for classical tomo-PIV algorithms (MART, BIMART and SMART): synthetic and experimental studies *Meas. Sci. Technol.* **25** 035303

Thomas L, Vernet R, Tremblais B and David L 2010 Influence of geometric parameters and image preprocessing on tomo-PIV results *15th Int. Symp. on Applications of Laser Techniques to Fluid Mechanics* (*Lisbon, Portugal, 5–8 July 2010*)

Tremblais B, David L, Arrivault D, Dombre J, Chatellier L and Thomas L 2010 SLIP: simple library for image processing (version 1.0) http://sliplib.prd.fr

Westerweel J and Scarano F 2005 Universal outlier detection for PIV data *Exp. Fluids* **39** 1096–100

Wieneke B 2008 Volume self-calibration for 3D particle image velocimetry *Exp. Fluids* **45** 549–56

Worth N A and Nickels T B 2008 Acceleration of Tomo-PIV by estimating the initial volume intensity distribution *Exp. Fluids* **45** 847–56

Worth N A, Nickels T B and Swaminathan N 2010 A tomographic PIV resolution study based on homogeneous isotropic turbulence DNS data *Exp. Fluids* **49** 637–56